J Electroceram (2007) 18:231–242
DOI 10.1007/s10832-007-9039-0

High amplitude vibration of piezoelectric bending actuators

T. Li · Y. H. Chen · F. Y. C. Boey · J. Ma

Received: 11 September 2005 / Accepted: 23 January 2007 / Published online: 8 February 2007

Abstract The properties of several configurations of piezoelectric bending actuators were investigated at high vibration amplitude both theoretically and experimentally. It was found that under high amplitude vibration conditions, the failure of the actuator was mainly caused by the maximum stress and domain reorientation. The actuator tends to fracture or crack at the location of maximum stress, which is indicated by the sudden drop of the displacement during frequency scan. The dimension, boundary condition and vibration order influence the distribution and magnitude of the stress. Domain reorientation may also occur during the frequency scan, which results in the distortion of the current profile. And meanwhile the magnitude of the current, admittance and temperature of the actuator will increase significantly and abruptly. The temperature was found to be increase with the increase of frequency, electric field or vibration amplitude due to the higher mechanical and electrical losses. The un-even stress distribution has also resulted in a high-to-low gradient temperature rise from the clamped end to the free end of the actuator under the Clamped-Free boundary condition. A linear model based on Euler–Benoulli theory has been derived and it provides reasonable explanations on the phenomena observed experimentally in this paper.

Keywords Piezoelectric · Bending actuator · Vibration

T. Li (✉) · Y. H. Chen · F. Y. C. Boey · J. Ma
School of Materials Science and Engineering,
Nanyang Technological University,
Nanyang Avenue,
Singapore 639798, Singapore
e-mail: Tli@ntu.edu.sg

1 Introduction

Piezoelectric actuators are largely applied in academic studies and industries due to their advantages of good displacement resolution, good mechanical durability, high speed, large output force and low power consumptions [1–6]. The piezoelectric actuators usually consist of the active components of piezoelectric ceramics (or single crystals, piezoelectric polymers, composites), passive components of substrate or elastic layer, and the controlling circuits. Two types of piezoelectric actuators, bending and multilayer actuators, have been well developed and widely used. Compared with the multilayer actuator, the bending actuator usually generates a lower blocking force but a much larger displacement.

The bending actuator consists of several configurations. The most commonly used are bimorph, unimorph, monomorph and tube. Figure 1 and Table 1 illustrate the configurations of these actuators. The bimorph actuator is usually fabricated by bonding two piezoelectric plates and driven by the opposite electric fields. In series bimorph (Fig. 1a), the upper and lower layer piezoelectric plates have antiparallel poling direction and the electric field is applied across the total thickness of the actuator. In the parallel bimorph (Fig. 1b), the upper and lower layer plates are poled in parallel direction and electric fields with the same magnitude and opposite polarity are applied to the individual plate. The unimorph actuator (Fig. 1c) is usually fabricated by bonding the piezoelectric plate to the elastic sheet. The piezoelectric plate is poled and driven by the electric field in the thickness direction. Monomorph (Fig. 1d) is a monolithic ceramic plate. In this paper, the technique of electrophoretic deposition (EPD) was applied to fabricate the monomorph actuator [7, 8]. Over the cross section of the actuator, the piezoelectric properties were

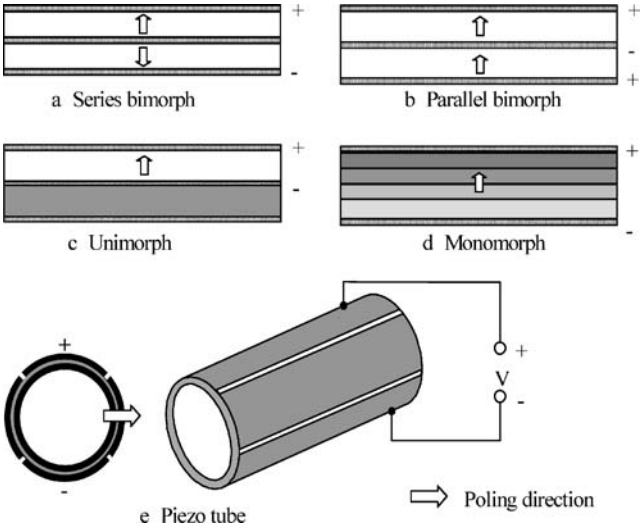

Fig. 1 Configurations of the studied piezoelectric bending actuators

made to vary in a graded manner. The actuator was poled in the thickness direction with the electric field applied between the top and bottom electrodes. The piezoelectric tube actuator (Fig. 1e) is a hollow tube and poled in the radial direction. The electrode in the outer surface is divided into four segments. When the electric field is applied across one of the opposing electrode segments, the actuator will perform the bending deformation.

There are large numbers of devices in practical applications, such as ultrasonic motors and ultrasound transducers. To achieve good performance, the actuator is required to work at high frequency and high amplitude conditions. However, operating in such conditions increases the risk of failure. Several factors, such as electric field, temperature, stress and frequency, could limit the performance of the piezoelectric actuators [9–21]. Electric field above the coercive field will switch the domain orientation; temperature above the Curie point will depole the sample; and stress above the strength will crack or break the sample. Frequency, on the other hand, will affect the vibration mode, vibration amplitude, stress distribution and electric properties of the actuator.

This paper studied the properties of bending actuators listed in Table 1 operating at high frequency and high vibration amplitude conditions. The purpose is to investigate the factors that limit the dynamic performance of the actuators. The vibration amplitude as a function of frequency (frequency response) and electric field (electric field response) was examined. A linear modal was also derived to explain and discuss the observed phenomena.

2 Linear theory of bending vibrations

2.1 Mechanical vibration

Euler–Benoulli beam theory was applied to analyze the vibration behavior of the bending actuators [22, 23]. For simplicity, only the bimorph actuator with Clamped-Free boundary condition at the first order vibration was considered. The dimension of the actuator is l in effective length, w in width, and 2 h in thickness. The governing equation of a vibrating actuator can be written as

$$EI\frac{\partial^4 u(x,t)}{\partial x^4} + C\rho A\frac{\partial u(x,t)}{\partial t} + \rho A\frac{\partial^2 u(x,t)}{\partial t^2} = f(x,t) \qquad (1)$$

where $u(x,t)$ is the bending displacement at position x and time t, C is the damping constant, E is the Young's modulus, I is the moment of inertia, ρ is the density, A is the area of cross section and $f(x,t)$ is the external distributed force. It has been known that the applied electric field $E_0e^{i\omega}$ is equivalent to a moment M_0 acted at the end of the bimorph actuator as [23]

$$M_0 = d_{31}E \cdot wh^2 \cdot E_0e^{i\omega t} \qquad (2)$$

In the above expression, d_{31} is the piezoelectric constant, E_0 is the magnitude of the electric field, and ω is the frequency of excitation. The solution of the above governing equation can then be expressed as

$$u(x,t,\omega) = \frac{0.334.l^2/h \cdot d_{31} \cdot Y(x)}{\sqrt{\left(1-(\omega/\omega_1)^2\right)^2 + 4\xi^2(\omega/\omega_1)^2}} E_0e^{i(\omega t-\phi)} \qquad (3)$$

Table 1 Configurations of the studied piezoelectric bending actuators.

Actuator	Structure	Poling direction	Electric field
Series bimorph	Two piezo plates bonded together	Antiparallel	Across the total thickness; Opposite electric field
Parallel bimorph	Two piezo plates bonded together	Parallel	Between intermediate and top/bottom electrodes; Opposite electric field
Unimorph	Piezo plate bonded to elastic sheet	Unidirectional	Across the piezo plate
Monomorph	Gradient piezoelectric properties over the cross section	Unidirectional	Across the total thickness
Piezo tube	Piezoelectric hollow tube	Radial	Across the opposing electrode segment

where ξ is the damping ratio. The phase lag ϕ, mode shape $Y(x)$ and the first order natural frequency ω_1 in the above equation are

$$\tan(\phi) = \frac{2\xi\omega_1\omega}{\omega_1^2 - \omega^2} \tag{4}$$

$$Y(x) = \cosh\lambda x - \cos\lambda x + \alpha(\sinh\lambda x - \sin\lambda x) \tag{5}$$

$$\omega_1 = \lambda_1^2\sqrt{\frac{EI}{\rho A}} \tag{6}$$

where

$$\begin{cases} \lambda_1 l = 1.875104 \\ \alpha = -0.734096 \end{cases} \tag{7}$$

$$I = \frac{2wh^3}{3} \tag{8}$$

The frequency response based on Eqs. 3 and 4 and mode shape of the actuator based on Eq. 5 have been shown in Fig. 2a and b, respectively. For the first order vibration, from the clamped end to the free end, the displacement increases monotonously as seen in Fig. 2b. The displacement is dependant on the frequency and damping ratio ξ of the actuator under the constant electric field condition as seen in Fig. 2a. At resonance, the displacement reaches maximum. Increasing the damping ratio, the vibration losses of the actuator increase. As a result, the amplitude of the resonant displacement decreases. Displacement measured experimentally was also compared with the theoretical values as shown in Fig. 2a. The damping ratio is estimated to be 0.064, which was determined by fitting the measured data to Eq. 3. It is noted that that experimental curve is narrower than the theoretical curve, which may be due to the fact that only the viscoelastic damping was considered in the model [22].

2.2 Electrical properties

(a) Electric displacement

The electric displacement, D_3, which is the measure of electric charges per unit area (charge density), can be obtained using the following equation

$$\begin{cases} D_3 = \dfrac{d_{31}}{s_{11}^E}S_1 - \dfrac{d_{31}^2}{s_{11}^E}E_3 + \varepsilon_{33}^T E_3 \\ S_1 = -z\dfrac{\mathrm{d}u^2}{\mathrm{d}x^2} \end{cases} \tag{9}$$

Where S_1 is the strain, E_3 is the electric field, S_{11}^E is the elastic compliance, z is the position in the thickness direction of the actuator. Replacing displacement u in the expression using Eq. 3, D_3 can be found to be

$$D_3 = \left\{ \begin{array}{l} -\dfrac{1.174\cdot k_{31}^2\varepsilon_{33}^T\cdot\cos\phi}{\sqrt{\left(1-(\omega/\omega_1)^2\right)^2 + 4\xi^2(\omega/\omega_1)^2}} \\ \quad (\cosh\lambda x + \cos\lambda x + \alpha(\sinh\lambda x + \sin\lambda x)) \\ -\varepsilon_{33}^T(1-k_{31}^2) \\ +i\dfrac{1.174\cdot k_{31}^2\varepsilon_{33}^T\cdot\sin\phi}{\sqrt{\left(1-(\omega/\omega_1)^2\right)^2 + 4\xi^2(\omega/\omega_1)^2}} \\ \quad (\cosh\lambda x + \cos\lambda x + \alpha(\sinh\lambda x + \sin\lambda x)) \end{array} \right\} E_0 e^{i\omega t} \tag{10}$$

The distribution of the electric displacement of the bimorph actuator at the resonant state has been shown in Fig. 2c. It can be seen that the electric displacement is not uniformly distributed. At the clamped end, the electric displacement is much larger than that at the free end. This is attributed to the curvature of the surface that affects the distribution of the surface charge. At the clamped end, the actuator has larger curvature than that in the free end. Increasing the damping ratio, similar as the vibration displacement, the magnitude of the electric displacement drops.

(b) Electric charge Q

Electric charge Q over the surface can be obtained as

$$Q = \int_0^w\int_0^l D_3\mathrm{d}x\mathrm{d}y = \left\{ \begin{array}{l} -\dfrac{0.920\cdot wl\cdot k_{31}^2\varepsilon_{33}^T\cdot\cos\phi}{\sqrt{\left(1-(\omega/\omega_1)^2\right)^2 + 4\xi^2(\omega/\omega_1)^2}} \\ \quad -\varepsilon_{33}^T(1-k_{31}^2)wl \\ +\dfrac{0.920\cdot wl\cdot k_{31}^2\varepsilon_{33}^T\cdot\sin\phi}{\sqrt{\left(1-(\omega/\omega_1)^2\right)^2 + 4\xi^2(\omega/\omega_1)^2}} \end{array} \right\} E_0 e^{i\omega t} \tag{11}$$

The frequency response of the surface charge has been shown in Fig. 2d. It can be seen that charge is not constant even under constant field driving conditions. It reaches maximum at the resonant frequency and attains minimum at the antiresonant frequency.

(c) Admittance

The admittance Y can be obtained from the ratio of the current I_c and the applied voltage $E_0 2he^{i\omega t}$

$$Y = \frac{I_c}{E_0 2he^{i\omega}} = \frac{\mathrm{d}Q/\mathrm{d}t}{E_0 2he^{i\omega}} = -\omega\frac{0.920\cdot k_{31}^2\varepsilon_{33}^T\cdot\sin\phi\cdot wl/2h}{\sqrt{\left(1-(\omega/\omega_1)^2\right)^2 + 4\xi^2(\omega/\omega_1)^2}} - i\omega\left\{\frac{0.920\cdot k_{31}^2\varepsilon_{33}^T\cdot\cos\phi\cdot wl/2h}{\sqrt{\left(1-(\omega/\omega_1)^2\right)^2 + 4\xi^2(\omega/\omega_1)^2}} + \varepsilon_{33}^T(1-k_{31}^2)\frac{wl}{2h}\right\} \tag{12}$$

The phase difference θ between the current and voltage is the imaginary part over the real part of the admittance, therefore

$$\tan\theta = \operatorname{ctan}\phi + \frac{\left(1-k_{31}^2\right)\sqrt{\left(1-(\omega/\omega_1)^2\right)^2 + 4\xi^2(\omega/\omega_1)^2}}{0.920\cdot k_{31}^2\cdot\sin\phi} \tag{13}$$

The variations of the admittance Y and phase θ as a function of frequency and damping ratio ξ have been shown in Fig. 2e. The peaks with maximum and minimum admittance indicate, respectively, the resonant and antiresonant frequency of the actuator. An experimental curve measured using HP4194A Impedance Analyzer is also shown in the Fig. 2e. The experimental data show consistent trend with that obtained from the theoretical analysis. However, the admittance is observed to be larger and the resonant frequency is slight lower than the theoretical predictions under the same damping conditions. Nevertheless, the resonant frequency is nearly 90% that of the theoretical value. To be more accurate, further investigation is required on the damping mechanism.

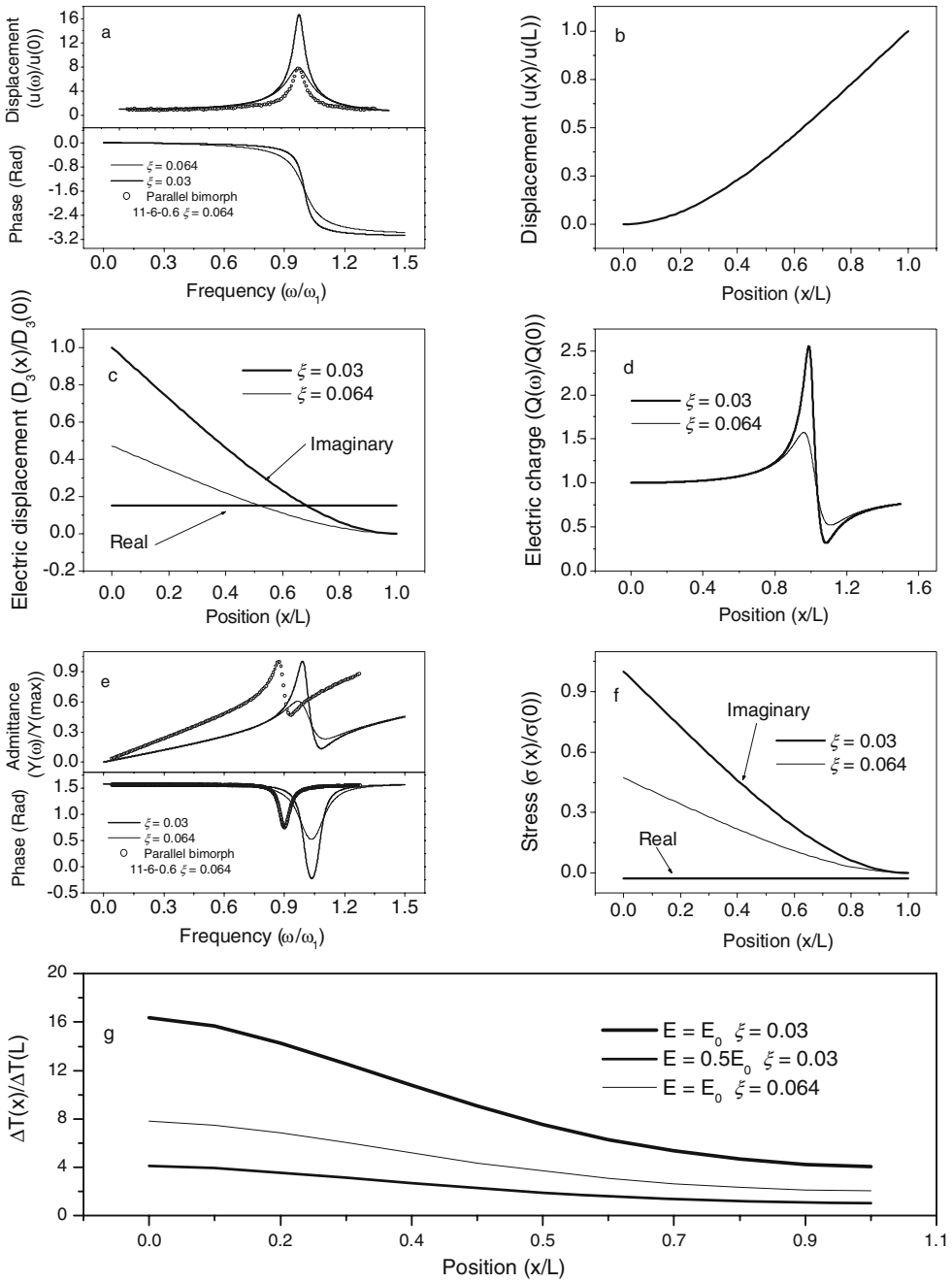

Fig. 2 Theoretical response of the piezoelectric bending actuators under clamped-free boundary condition

2.3 Stress distribution

Using the classical relation

$$T_1 = \frac{S_1}{s_{11}^E} - \frac{d_{31}}{s_{11}^E} E_3 \tag{14}$$

and the second expression of Eq. 9, the stress distribution of a bending actuator can be obtained as

$$T_1 = \left\{ \begin{array}{l} -\dfrac{1.174 \cdot \cos\phi \cdot d_{31}/s_{11}^E}{\sqrt{\left(1-(\omega/\omega_1)^2\right)^2 + 4\xi^2(\omega/\omega_1)^2}} \\ (\cosh\lambda x + \cos\lambda x + \alpha(\sinh\lambda x + \sin\lambda x)) + \dfrac{d_{31}}{s_{11}^E} \\ +i\dfrac{1.174 \cdot \sin\phi \cdot d_{31}/s_{11}^E}{\sqrt{\left(1-(\omega/\omega_1)^2\right)^2 + 4\xi^2(\omega/\omega_1)^2}} \\ (\cosh\lambda x + \cos\lambda x + \alpha(\sinh\lambda x + \sin\lambda x)) \end{array} \right\} E_0 e^{i\omega t} \tag{15}$$

Figure 2f shows the stress distribution of the actuator at the resonant frequency. It can be found that the maximum stress takes place at the clamped end of the actuator, and diminishes gradually towards the free end. Reducing the damping ratio, the vibration amplitude increases. As a result, the stress level is also found to be increased.

2.4 Heat generation

Heat generation is caused by the electrical and mechanical losses during the vibration of the actuators. The temperature rise is not evenly distributed over the surface of the actuator. Assuming heat generation is one-dimensional, and considering conservation of energy, the governing equation for the heat generation at steady state can be derived to be [24–29]

$$Ak\frac{d^2\Delta T}{dx^2} - A_c h'\Delta T + AQ_{\text{gen}} = 0 \tag{16}$$

where A is the area of the cross section, A_c is the perimeter of the vibrating actuator, ΔT is the temperature rise, k is the thermal conductivity (W/m°C) (typical values of the thermal conductivity for PZT materials are k=1.25 W/m°C [24]), h' is the heat transfer coefficient (h' has the magnitude of 6–30 W/(m^2°C) for free convection in air [26]). For piezoelectric materials, there exists

$$Q_{\text{gen}} = Q_{\text{mec}} + Q_{\text{ele}} \tag{17}$$

where Q_{mec} and Q_{ele} are the mechanical and electrical loss per unit volume, respectively. The electrical loss is dissipated evenly throughout the actuator [24]. The mechanical loss is proportional to the mechanical stress of the sample as shown below [22, 29]

$$Q_{\text{mec}} = \frac{1}{2}\omega s_{11}^E T_1^2 \tan\delta_m \tag{18}$$

where $\tan\delta_{\text{m}}$ is the mechanical loss tangent and is equal to $1/Q_m$, here Q_m is the mechanical quality factor.

The dissipated power density of an actuator due to electrical loss is [3, 29],

$$Q_{\text{ele}} = \frac{1}{2}E_0^2\omega\varepsilon\tan\delta \tag{19}$$

For simplicity, only the heat generation at natural frequency ω_1 was considered in the following derivations. Considering the stress distribution derived earlier and also defining the following parameters

$$\left\{ \begin{array}{l} C: \text{constant respresenting magnitude of the stress} \\ D = E_0 d_{31}/s_{11}^E \\ E = \dfrac{1}{2}AE_0^2\omega\varepsilon\tan\delta \\ B = \dfrac{1}{2}A\omega s_{11}^E\tan\delta_m \\ F = BC^2 \\ J = F + BD^2 + E \end{array} \right. \tag{20}$$

Eq. 16 becomes

$$\begin{array}{l} -Ak\dfrac{d^2\Delta T}{dx^2} + A_c h'\Delta T \\ = \left\{ \begin{array}{l} A\dfrac{1}{2}\omega s_{11}^E\tan\delta_m\left\{\sqrt{(C(\cosh\lambda x + \cos\lambda x + \alpha(\sinh\lambda x + \sin\lambda x)))^2 + D^2}\right\}^2 \\ +A\dfrac{1}{2}E_0^2\omega\varepsilon\tan\delta \end{array} \right\} \end{array} \tag{21}$$

Solving the above equation, the temperature rise can be obtained to be

$$\begin{array}{l} \Delta T = C_1 e^{\sqrt{A_c h'/Ak}x} + C_2 e^{\sqrt{A_c h'/Ak}x} + \dfrac{F(1+\alpha)^2}{-16Ak\lambda^2 + 4A_c h'}e^{2\lambda x} \\ \quad + \dfrac{F(1-\alpha)^2}{-16Ak\lambda^2 + 4A_c h'}e^{-2\lambda x} + \left(\dfrac{F(1+\alpha)(-\alpha A_c h' + 2Ak\lambda^2)}{-4A^2k^2\lambda^4 - A_c^2 h'^2}\right)e^{\lambda x}\sin\lambda x \\ \quad + \dfrac{F(1+\alpha)(-A_c h' - 2\alpha Ak\lambda^2)}{-4A^2k^2\lambda^4 - A_c^2 h'^2}e^{\lambda x}\cos\lambda x \\ \quad + \dfrac{F(1-\alpha)(-A_c h' + 2\alpha Ak\lambda^2)}{-4A^2k^2\lambda^4 - A_c^2 h'^2}e^{-\lambda x}\cos\lambda x \\ \quad + \dfrac{F(1-\alpha)(-\alpha A_c h' - 2Ak\lambda^2)}{-4A^2k^2\lambda^4 - A_c^2 h'^2}e^{-\lambda x}\sin\lambda x \\ \quad + \dfrac{F(1-\alpha)^2}{8Ak\lambda^2 + 2A_c h'}\cos 2\lambda x + \dfrac{\alpha F}{4Ak\lambda^2 + A_c h'}\sin 2\lambda x + \dfrac{J}{A_c h'} \end{array} \tag{22}$$

To determine the unknowns C_1 and C_2, the following boundary condition can be applied

$$-Ak\frac{d\Delta T}{dx} = Ah'\Delta T\Big|_0^l \tag{23}$$

It indicates that at the two ends of the actuator the heat conducted through the end surfaces is equal to the heat dissipated from the same surface. Defining the following parameters

$$\begin{cases} A_1 = \sqrt{\dfrac{A_c h'}{Ak} + \dfrac{h'}{k}} \\ A_2 = \left(-\sqrt{\dfrac{A_c h'}{Ak}}\right) + \dfrac{h'}{k} \\ A_3 = \left(-\dfrac{h'}{k}\Delta T0\right) - d\Delta T0 \\ A_4 = \sqrt{\dfrac{A_c h'}{Ak}} e^{\sqrt{\frac{A_c h'}{Ak}}l} + e^{\sqrt{\frac{A_c h'}{Ak}}l}\left(\dfrac{h'}{k}\right) \\ A_5 = \left(-\sqrt{\dfrac{A_c h'}{Ak}}\right) e^{-\sqrt{\frac{A_c h'}{Ak}}l} + e^{-\sqrt{\frac{A_c h'}{Ak}}l}\left(\dfrac{h'}{k}\right) \\ A_6 = \Delta Tl\left(-\dfrac{h'}{k}\right) - d\Delta Tl \end{cases} \tag{24}$$

and taking Eq. 22 into 23, the unknown parameters can be obtained as

$$\begin{cases} C_1 = \dfrac{A_2A_6 - A_3A_5}{A_2A_4 - A_1A_5} \\ C_2 = \dfrac{A_3A_4 - A_1A_6}{A_2A_4 - A_1A_5} \end{cases} \tag{25}$$

Figure 2g illustrates the temperature rise along the length of the actuator. It can be found that the maximum temperature rise happens at the clamped end. This is consistent with the position of the maximum stress, which induces maximum mechanical loss as that indicated from Eq. 18 and Fig. 2f. The temperature rise decreases gradually to the free vibration end of the actuator. The magnitude of the temperature rise depends both on the electric field and damping ratio. As damping ratio decreases, the vibration displacement and magnitude of stress increase. As a result, the mechanical loss increases, which induces the increase of the temperature rise. Unlike the vibration displacement (Eq. 3), electric displacement (Eq. 10), charges (Eq. 11) and stress (Eq. 15), the temperature rise is not linearly proportional to the electric field. As seen in Fig. 2g, as electric field reduces by half, the temperature rise will reduce to nearly a quarter of the original value. This is because both electrical loss and mechanical loss are proportional to the square of the electric field as indicated from Eqs. 18 and 19.

3 Experimental

Both commercial and self-fabricated actuators were applied in this work. The series and parallel bimorph were from Morgan Electro Ceramics with material PXE5. The piezo tube was from the BPO Boston Piezo-Optics Inc with material Navy type III. The monomorph, unimorph and parts of the series bimorph were self-fabricated. The monomorph was fabricated using the EPD technique [7, 8]. Two starting materials PZT0 and PZT1 with different piezoelectric properties were mixed, deposited and co-sintered [7, 8]. Due to the variation of the material compositions, the graded piezoelectric properties result in differential expansion or shrinkage over the cross section of the actuator when electric field is applied across the total thickness. The net result is the bending movement of the actuator. The unimorph was made by applying the soldering tin on one side of the piezo plate, where the soldering tin works as the elastic layer. The self-fabricated series bimorph was made of material PZT1 by bonding two piezoelectric plates using the silver paste. The fabricated monomorph, unimorph and series bimorph actuator were poled under 2 kV/mm at 100°C in silicone oil for 30 min. The material properties and dimensions of the studied piezoelectric actuators are listed in Tables 2 and 3, respectively. In Table 3, the dimensions of the actuators are represented by *L-W-T* (mm^3), where *L* is the effective length, *W* is the width and *T* is the thickness. For piezo tube actuator, *L*, *W* and *T* represent length, outer diameter and wall thickness, respectively.

The performance of the bending actuator was measured using the setup as shown in Fig. 3. It consists of Vibraplane (RS Kinetic Systems, Inc.), MTI-2000 fotonic sensor (probe: MTI2032RX, MTI Instruments), FG3000 function generator (Yokogawa), PZD2000 high voltage amplifier

Table 2 Material properties of the studied bending actuators.

Materials	ρ (g/cm^3)	Q_m	tanδ	s_{11}^E(10^{-12} /Pa)	$\varepsilon_{33}^T/\varepsilon_0$	d_{31} (10^{-12} m/V)
PXE5	7.8	75	0.02	15	2,100	−215
PZT1	7.6	–	–	11	688	−99.5
PZT0	7.4	–	–	18	719	−62.5
Navy Type III	7.5	1,000	0.004	10	1,000	−97

Table 3 Summary of dimensions, test conditions and properties of the studied actuators.

Actuators	Materials	Dimension *L-W-T* (mm^3)	Boundary condition	Vibration order	Failure mode	Failure field (V_{p-p}/mm)	Maximum displacement (μm_{p-p})
Series bimorph	PXE5	8-4-0.6	Clamped-Free	1st	Stress	833	187[a]
		35-1.6-0.6	Free–Free	1st	Stress	500	304[b]
	PZT1	4-2.7-0.17	Clamped-Free	1st	Stress	824	80
		6-2.75-0.17	Clamped-Free	1st	Stress	706	212
		8-2.36-0.17	Clamped-Free	1st	Stress	588	354
		8-2.22-0.62	Clamped-Free	1st	Stress	806	202
Parallel bimorph	PXE5	11-6-0.6	Clamped-Free	1st	Stress	667	103[c]
Piezo tube	Navy type	30-5-0.75	Clamped-Free	1st	Stress	3,467	183
	III	30-5-0.75	Clamped-Free	2nd	Stress	1,867	30
Unimorph	PZT1	10.13-2.59-0.66 (pzt 0.28 mm)	Clamped-Free	1st	Domain reorientation	2,857	315
Monomorph	PZT1+PZT0	10-2.6-0.26	Clamped-Free	1st	Domain reorientation	3,077	364

[a] Displacement was measured at location 4 mm from the clamped end.
[b] Displacement was measured 3 mm from the clamped end.
[c] Displacement was measured at the middle of the actuator to avoid out of measurement range of the displacement sensor.

(Trek), DL1640L oscilloscope (Yokogawa) and IRI 1011 thermal imager (IRISYS). Function generator and voltage amplifier were the driving system and provided sinusoidal signals. The bending displacement was measured under the Clamped-Free boundary condition. The fotonic sensor was used to measure the displacement. And the data were recorded using the oscilloscope. The thermal imager was connected to a PC and applied to examine the temperature rise and temperature distribution in the sample.

The electric field and frequency response of the actuator were examined as follows: at a constant electric field, a frequency scan was carried out from the frequency much lower than the resonance to a frequency over the first order resonance. Then a new frequency scan was performed at an elevated electric field level. This procedure was repeated until the observation of the component failure.

4 Results and discussion

The actuators applied in this study have been summarized in Table 3. The failure mode, failure field and maximum displacement achieved before failure have been listed. It was found that there are two major effects that caused the failure of the actuators. In series, parallel bimorph and piezo tube actuator, the samples were found to fracture at the position of maximum stress. In the unimorph and monomorph actuator, the effect of domain reorientation was observed.

4.1 Effect of stress

Figure 4a shows the electric field and frequency response of the series bimorph. The measurement started at 167 Vp-p/mm and the sampled failed at 833 Vp-p/mm. The variation of the displacement is similar as that of the theoretical analysis as seen in Fig. 2a. However due to the non-linearity at high field driving conditions, the shapes of the curves deviate from that identified at the low field condition and become more asymmetrical as electric field increases. The displacement increases with the increase of the applied electric field. However, the increase is not ideally linear as that revealed in Eq. 3. This is because both mechanical and electrical losses will increase as indicated in Eqs. 18 and 19 when the electric field increases. As a result, the damping ratio ξ in Eq. 3 increases. As discussed earlier, the increase of the damping ratio will in turn decrease the resonant displacement. Furthermore, it will also cause the resonant peak shift towards the lower frequency end as shown in the Fig. 4a. At 500 Vp-p/mm, the displacement is observed to drop suddenly after passing the resonance point. The effect became more obvious when the electric field is further increased, and fracture can be found at the clamped end as shown in Fig. 5a. Therefore, the sudden drop of the displacement during the frequency scan indicates the crack generation or fracture of the samples.

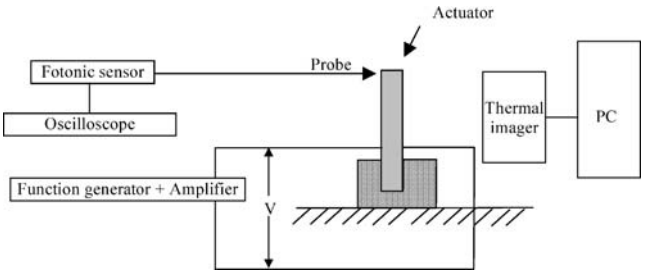

Fig. 3 Characterization setup of the bending actuators

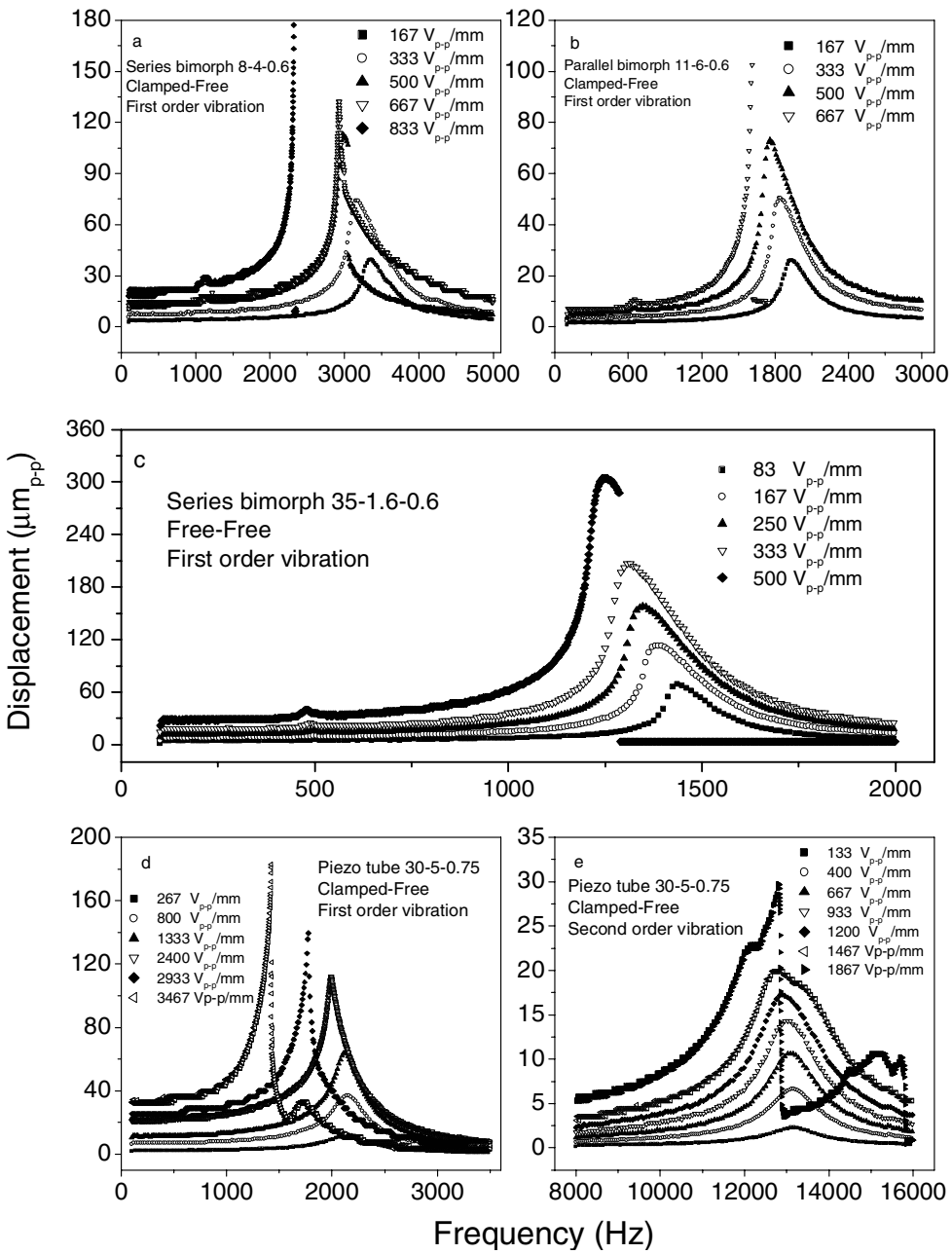

Fig. 4 Frequency and electric field response of the piezoelectric bimorph and tube actuators

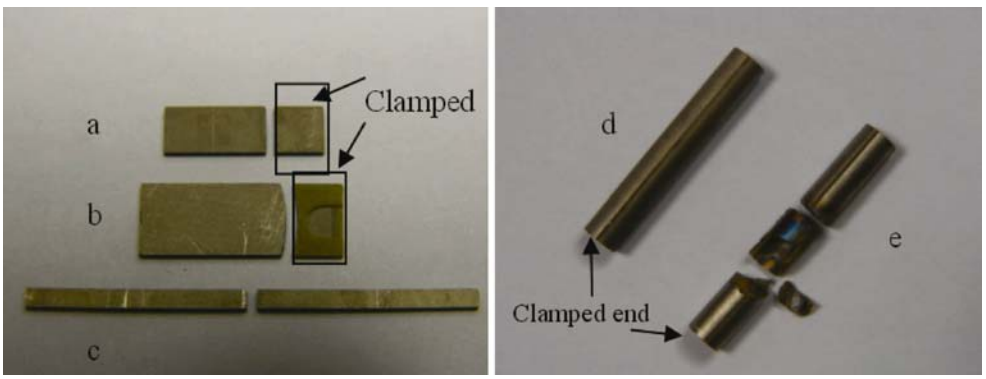

Fig. 5 Fracture of bimorph and piezo tube actuators **a** series bimorph 8-4-0.6 (clamped-free, first order vibration), **b** parallel bimorph 11-6-0.6 (clamped-free, first order vibration), **c** series bimorph 35-1.6-0.6 (free–free, first order vibration) **d** piezo tube 30-5-0.75 (clamped-free, first order vibration) and **e** piezo tube 30-5-0.75 (clamped-free, second order vibration)

As analyzed earlier, the maximum stress appears at the clamped end of the actuator as shown in Fig. 2f. As a result, the fracture likely occurs there once the maximum stress exceeds the strength of the materials. Figure 4b illustrates the field and frequency response of the parallel bimorph. Similar phenomenon as that of the series bimorph has been observed. The sudden drop of the displacement took place at 667 Vp-p/mm, and the sample was found to fracture at the same location of the clamped end as seen in Fig. 5b. Figure 4d shows the result of the piezo tube actuator. The sudden drop phenomenon was found at a much higher electric field of 3,467 Vp-p/mm. However, the fracture of the sample was not seen as that in Fig. 5d. This may be due to higher rigidity and bending stiffness of the tubular structure. However, from the sudden drop of the displacement, it can be deduced that the crack generation has started.

The stress level and stress distribution are affected by the boundary condition, vibration order and dimension of the actuator. Fig. 4c shows the frequency response of a series bimorph under the Free–Free boundary conditions. Compared with the situation of Clamped-Free, fracture took place at the middle part of the actuator as seen in Fig. 5c. This is because under this condition, the maximum stress arises at the middle of the actuator. Figure 4e is the second order vibration of the piezo tube. In contrast to the first order vibration (Fig. 4d), the fracture occurred in the middle part. There are two stress peaks for the second order vibration, the clamped end and the middle part (0.52l from the clamped end). In the present case, the tube broke near the location of the second stress peak. Figure 6 illustrates the effect of dimension on the stress level of the actuator. The bimorphs were fabricated using the material PZT1. It was found that longer and thinner actuator generates larger displacement than thicker and shorter actuators. This is because longer and thinner actuators have lower stress levels under the same displacement conditions and hence produces larger displacement than the shorter and thicker ones.

4.2 Effect of domain reorientation

In the unimorph and monomorph actuator, the effect of domain reorientation was observed instead of fracture of the actuator. The domain reorientation can be deduced from the measurement of the current as seen in Fig. 7a. Before domain reorientation, the direction of polarization does not change as seen in Fig. 7b and the current varies sinusoidally. However, once domain reorientation takes place, above the coercive field, domains are switched to the opposite direction following the variation of the electric field as seen in Fig. 7c. As a result, the current profile distorts significantly as shown in Fig. 7a. In addition, sharp peaks can also be observed in the current profile. It is known that during domain reorientation, the surface charge varies abruptly. As discussed earlier that $I_c = dQ/dt$, hence the abrupt change of the surface charge will induce the current peaks as observed in the figure. Therefore, from the current distortion and peaks of the current profile, the domain reorientation can be deduced.

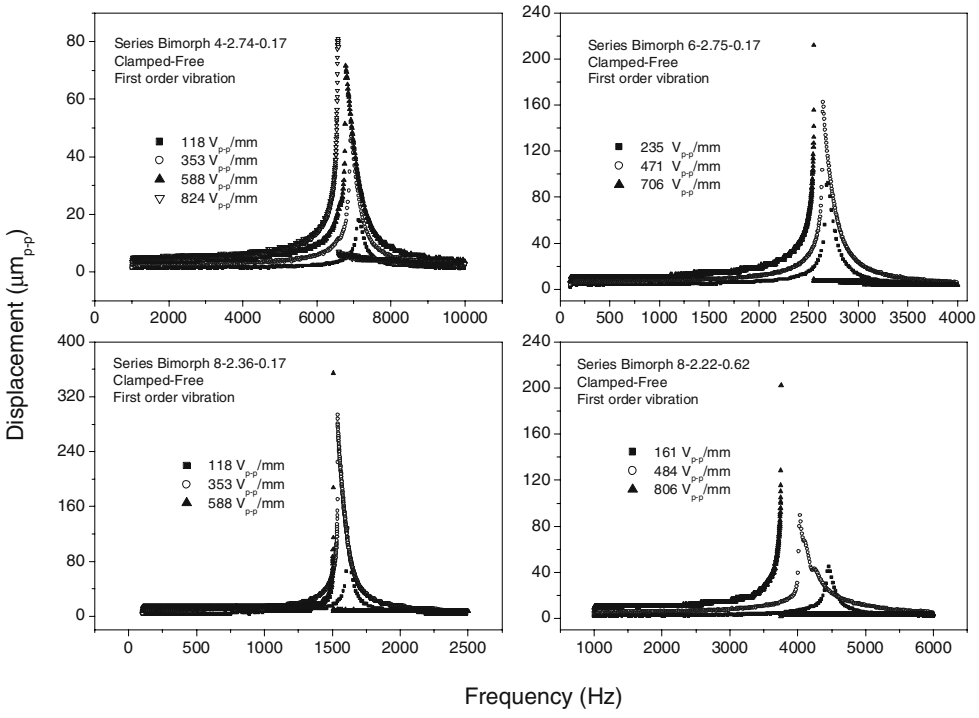

Fig. 6 Frequency and electric field response of PZT1 bimorphs with different dimensions

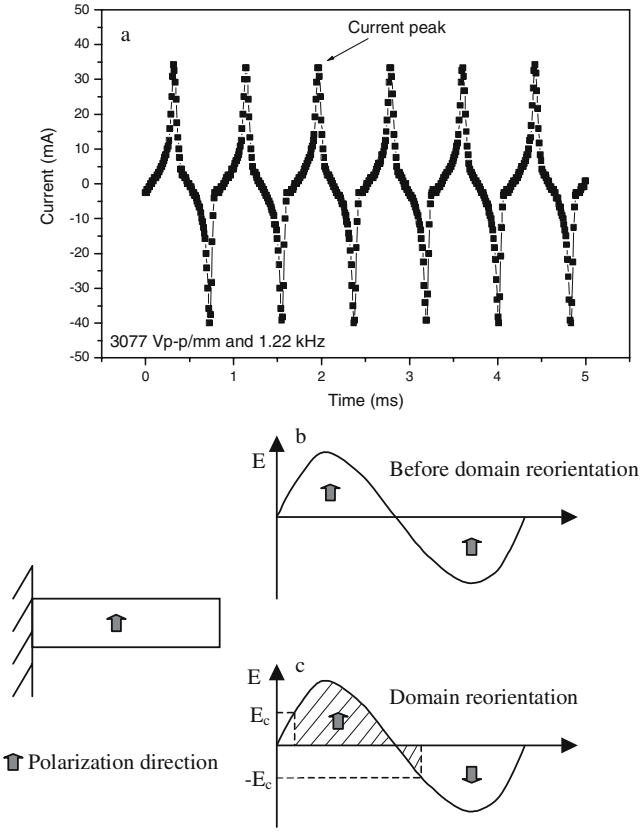

Fig. 7 Current profile of monomorph 10-2.60-0.26 during domain reorientation

Figure 8 shows the electric field and frequency response of a unimorph actuator. The variation of the current and voltage at 2,857 Vp-p/mm are also shown, where the domain reorientation is observed. As seen in Fig. 8, as electric field increases to 2,857 Vp-p/mm, there is a sudden jump of the displacement above the resonant frequency. Meanwhile, the similar current distortion and current peaks as shown in Fig. 7a were observed. The magnitude of the current also increased abruptly. The distortion and sharp increase of the current peaks as discussed earlier are resulted from the domain reorientation.

It should be noted that the domain reorientation did not arise at the initial stage but occurs at the later stage the frequency scan. This frequency dependent phenomenon of the domain reorientation deserves further study. There exist several possibilities that may contribute to this effect. Firstly, as theoretically analyzed earlier, both mechanical loss and electrical loss will turn to heat eventually. The heat then lowers the coercive field, eases and accelerates the domain reorientation. Furthermore, both mechanical and electrical losses are proportional to the frequencies as seen in Eqs. 18 and 19. Hence, the domain reorientation may happen at higher frequencies rather than the initial stage of frequency scan. Secondly, as seen in Fig. 2c, the surface charge density D_3 is not evenly distributed. At the clamped end, the charge density is larger than other positions. So even the electric field is lower than the coercive field, the local charge density at the clamped end may have exceeded the cutoff value. This forces the domains to switch to produce more charges to compensate that at the high density locations. The third reason may be that the high frequency and repeated action of the actuator reduce the

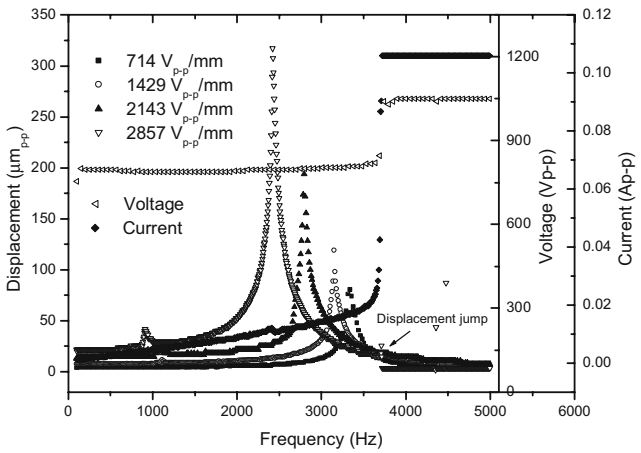

Fig. 8 Frequency and electric field response of unimorph 10.13-2.59-0.66 (pzt 0.28 mm)

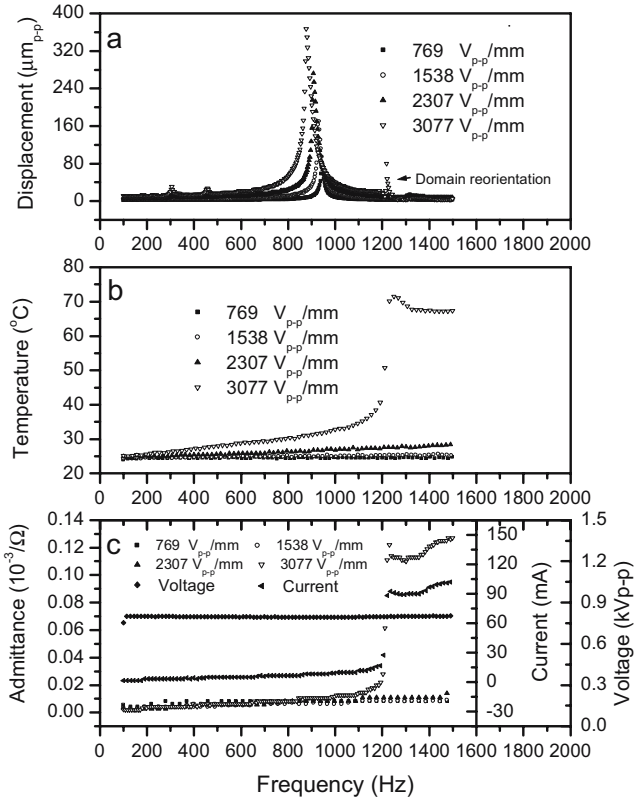

Fig. 9 Frequency and electric field response of monomorph actuator 10-2.60-0.26

barrier and resistance of the domain reorientation. It was reported that if an electric field lower than coercive field is applied over a long time, the polarization will eventually switch [30].

Figure 9 shows the electric field and frequency response of a monomorph actuator. The voltage, current, admittance, and temperature rise are also shown in the figure. The domain reorientation took place at voltage 3,077 Vp-p/mm and a frequency above the resonance. Before domain reorientation, there was a slight increase of the admittance and current. Similar trend is also observed in the unimorph actuator as shown in Fig. 8. This is because the admittance is proportional to the driving frequencies as shown in Eq. 12. After domain reorientation, as that in the case of unimorph, the magnitude of the current increases significantly and abruptly. The temperature was observed to increase with the frequency and electric field as shown in Fig. 9b. This is because both mechanical and electrical losses increase with the driving frequency and electric field as represented in Eqs. 18 and 19. However, the temperature rise is negligible compared with that observed after domain reorientation has occurred. This indicates that during the domain reorientation, there are huge amount of losses that results in high heat generation.

Figure 10 shows the temperature distribution of the actuator at 3,077 Vp-p/mm and various frequencies during the frequency scan. The theoretical analysis earlier indicates that there is a gradual decrease of the temperature from the clamped end to the free end of the actuator as seen in Fig. 2g. The experimental observations are consistent with

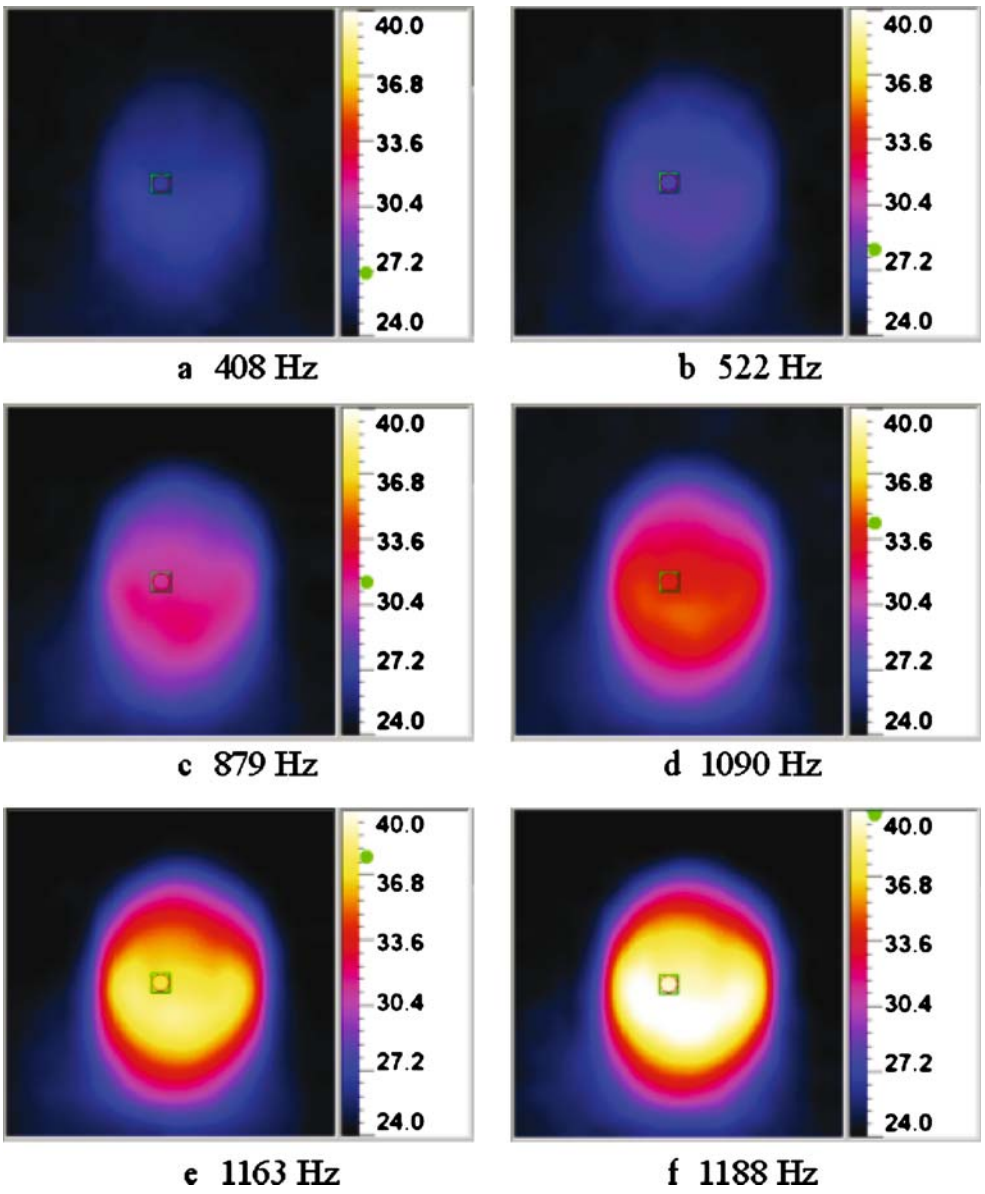

Fig. 10 Temperature distribution of monomorph 10-2.60-0.26

that derived from the theoretical analysis where the lower temperature is observed at the free end (upper side in the figure) and higher temperature near the clamped end. This is the result of stress distributions as shown in Fig. 2f, where larger mechanical loss is noted at the clamped end than that at the free end of the actuator.

5 Conclusions

Several configurations of bending actuators, including series bimorph, parallel bimorph, unimorph, monomorph and piezo tube, were investigated at high vibration amplitude. A linear theory based on Euler–Benoulli beam model has been derived in this work. The derived expressions provides good descriptions and explanations on the phenomena observed experimentally. It was found that the failure of the actuator was mainly caused by stress and domain reorientation. The stress is distributed gradely along the actuator. For Clamped-Free boundary condition, the magnitude of the stress decreases from the clamped end to the free end. The boundary conditions, vibration order and dimensions are the important factors that influence the distribution and magnitude of the stress. The actuator tends to fracture or crack at the location of maximum stress. The cracking or fracture of the actuator can be confirmed by the sudden drop of the displacement. This is likely to happen near the resonance due to large magnitude of the stress induced. Domain reorientation may also occur during the frequency scan, which can be confirmed from the current distortion, current peak and sudden increase of the magnitude of the current or admittance observed during the measurement. Large losses will generate upon domain reorientation, and in turn induce abrupt and significant increase in temperature. On the other hand, as frequency, electric field or vibration amplitude increase, the losses will also increase. This could result in more heat generation and larger temperature rise. In the Clamped-Free boundary condition, the maximum temperature is noted to happen near the clamped end due to the maximum mechanical loss there. As the position moves towards the free end, temperature rise decreases.

References

1. C. Niezrechi, D. Brei, A. Moskalik, Shock Vibr. Dig. **33**, 269 (2001)
2. G.H. Haertling, J. Am. Cram. Soc. **82**, 797 (1999)
3. A.J. Moulson, J.M. Herbert, *Electroceramics*. (Wiley, England, 2003), Chapter 2 & 6
4. J.G. Smits, S.I. Dalke, T.K. Cooney, Sens. Actuators **28**, 41 (1991)
5. M. Besell, S. Johansson, Journal of Electroceramics **3**, 73 (1999)
6. J.H. Yoo, J.I. Hong, W. Cao, Sens. Actuators **79**, 8 (2000)
7. Y.H. Chen, T. Li, J. Ma, in *Proceedings of the International Conference on Smart Materials-Smart/Intelligent Materials and Nanotechnology* (Chiang Mai University, Thailand, 2004), p. 70
8. T. Li, Y.H. Chen, J. Ma, J. Mater. Sci. **40**, 3601 (2005)
9. T. Kanda, Y. Kobayashi, T. Higuchi, Jpn. J. Appl. Phys. **42**, 3014 (2003)
10. M. Umeda, K. Nakamura, S. Ueha, Jpn. J. Appl. Phys. **38**, 5581 (1999)
11. S. Tashiro, M. Ikehiro, H. Igarashi, Jpn. J. Appl. Phys. **36**, 3004 (1997)
12. W.P. Chen, C.P. Chong, P.C.K. Liu, Mat. Sci., Eng. **B99**, 203 (2003)
13. C.H. Xu, J.H. Hu, H.L.W. Chan, Ultrasonics **39**, 735 (2002)
14. J.M. Calderon-Moreno, M. Popa, Mat. Sci. Eng. **A336**, 124 (2002)
15. T. Fett, D. Munz, G. Thun, J. Mater. Sci. Lett. **19**, 1921 (2000)
16. K. Uchino, J.H. Zheng, J.W.C. DE Vries, Journal of Electroceramics **2**, 33–40 (1998)
17. S. Takahashi, Y. Sasaki, K. Uchino, Jpn. J. Appl. Phys. **34**, 5328 (1995)
18. K. Uchino, S. Hirose, IEEE Trans. Ultrason. Ferroelectr. Freq. Control **48**, 307 (2001)
19. S. Takahashi, S. Hirose, K. Uchino, J. Am. Ceram. Soc. **77**, 2429 (1994)
20. Q.M. Wang, Q.M. Zhang, L.E. Cross, J. Appl. Phys. **86**, 3352 (1999)
21. Y. Sasaki, M. Umeda, M. Yamamoto, Jpn. J. Appl. Phys. **40**, 5743 (2001)
22. C.W. de Silva, *Vibration: Fundamentals and Practice*. (CRC, Boca Raton, 1999), p. 352
23. P. Lu, K.H. Lee, J. Sound Vib. **266**, 723 (2003)
24. S. Sherrit, X. Bao, Y. Bar-Cohen, in *Proceedings of the IEEE Ultrasonics Symposium*. (Institute of Electrical and Electronics Engineers Inc., Atlanta, 2001), P. 1097
25. J. Hu, IEEE Trans. Ultrason. Ferroelectr. Freq. Control **50**, 594 (2003)
26. J. Zheng, S. Takahashi, K. Uchino, J. Am. Ceram. Soc. **79**, 3193 (1996)
27. K. Yao, K. Uchino, L.C. Lim, IEEE Trans. Ultrason. Ferroelectr. Freq. Control **47**,819 (2000)
28. P. Kielczynski, W. Pajewski, Sens. Actuators **36**, 97 (1993)
29. P. Gerthsen, K.H. Hardtl, N. A. Schmidt, J. Appl. Phys. **51**, 1131 (1980)
30. D. Damjanovic, Rep. Prog. Phys. **61**, 1267 (1998)